

Lunar magnetic field measurements with a cubesat

Ian Garrick-Bethell^{*a,b}, Robert P. Lin^{c,b}, Hugo Sanchez^d, Belgacem A. Jaroux^d, Manfred Bester^e, Patrick Brown^f, Daniel Cosgrove^e, Michele K. Dougherty^f, Jasper S. Halekas^e, Doug Hemingway^a, Paulo C. Lozano^g, Francois Martel^h, Caleb W. Whitlock^g

^aDept. of Earth and Planetary Sciences, University of California, Santa Cruz, 1156 High Street, Santa Cruz, CA, USA 95064; ^bSchool of Space Research, Kyung Hee University, Yongin, Gyeonggi 446-701, Republic of Korea; ^cDept. of Physics, University of California, 7 Gauss Way, Berkeley, Berkeley, CA, USA 94720; ^dNASA Ames Research Center, Moffett Field, CA, USA 94035, ^eSpace Sciences Laboratory, University of California, Berkeley, 7 Gauss Way, Berkeley, CA, USA 94720, ^fSpace and Atmospheric Physics, The Blackett Laboratory, Imperial College, London, UK, SW7 2AZ, ^gDept. of Aeronautics and Astronautics, Massachusetts Institute of Technology, 77 Massachusetts Avenue, Cambridge, MA 02139, ^hEspace Inc., 30 Lynn Ave., Hull, MA, USA 02045.

*igarrick@ucsc.edu, phone: 831-459-1277

ABSTRACT

We have developed a mission concept that uses 3-unit cubesats to perform new measurements of lunar magnetic fields, less than 100 meters above the Moon's surface. The mission calls for sending the cubesats on impact trajectories to strongly magnetic regions on the surface, and transmitting measurements in real-time to a nearby spacecraft, or directly to the Earth, up until milliseconds before impact. The cubesats and their instruments are partly based on the NSF-funded CINEMA cubesat now in Earth orbit. Two methods of reaching the Moon as a secondary payload are discussed: 1) After launching into geostationary transfer orbit with a communication satellite, a small mother-ship travels into lunar orbit and releases the cubesats on impact trajectories, and 2) The cubesats travel to the Moon using their own propulsion after release into geosynchronous orbit. This latter version would also enable other near-Earth missions, such as constellations for studying magnetospheric processes, and observations of close-approaching asteroids.

Keywords: Moon, magnetism, solar wind, cubesat, impactor, CINEMA, electrospray.

1. INTRODUCTION AND OBJECTIVES

1.1 Introduction

This paper describes a 3U ($3U = 30 \times 10 \times 10$ cm) cubesat mission to make near-surface measurements of magnetic portions of the Moon that have remained a puzzle since the Apollo era. This mission, known as Lunar Impactor, would carry with it a flight-tested magnetometer as the minimum payload, but solar wind and dust sensors are also plausible and useful. In Section 1 we discuss the science and trajectory requirements that drive the Lunar Impactor mission. In Section 2 we discuss the magnetometer and a preliminary design for a solar wind sensor. In Sections 3 and 4 we discuss two mission-level architectures that could be used to implement Lunar Impactor: 1) A small mother-ship that releases cubesats on impact trajectories from lunar orbit, and 2) A fully-independent 3-axis stabilized cubesat that starts in geosynchronous orbit (GEO) and transfers to a lunar impactor trajectory using its own propulsion. In Sections 5 and 6 we address some of the technology that enables a cubesat mission of this class: communication and navigation via large ground stations, and high-specific impulse (I_{sp}) ion electrospray propulsion. In Section 7 we show trajectory simulations using the electrospray propulsion system. In Section 8 we conclude that flight of either mission architecture is possible with emerging technology within the next ~2 years. The platform behind Lunar Impactor would not only be useful for lunar science, but also as a versatile high delta- v platform capable of other missions in near-Earth space.

1.2 Science background and mission concept

The origin of lunar magnetism is one of the oldest problems in lunar science^{1,2}. Its study dates to the first object to leave the Earth: the Soviet Luna-1 in 1959. Luna-1 carried with it no cameras, but it carried a magnetometer to determine if

the Moon has a global magnetic field like the Earth's. Luna-1 found no global magnetic field, but 12 years later scientists were surprised to find that the Apollo 15 and 16 subsatellites had detected small (~100 km) patches of strongly magnetized material throughout the Moon's crust (Fig. 1). The dominant hypotheses for the formation of these magnetic "anomalies" suggest they are from either the magnetic field of an ancient lunar dynamo³⁻⁶, or processes related to the formation of plasmas produced during meteoroid impacts⁷. Solving this puzzle would help determine how the Moon fits into the spectrum of planetary magnetism observed across our solar system and galaxy. From neutron stars to Jupiter's icy satellite Ganymede, many bodies can generate dynamos. Yet, we barely know if, when, or how our moon ever generated one.

Deepening the mystery behind these magnetic patches is that some are co-located with unusual, brightly colored terrain⁸ (Fig. 2), known as "swirls." One leading explanation for this bright terrain is that solar wind protons, normally a darkening agent, are being deflected by the magnetic field, and keeping the underlying surface bright^{8,9}. If true, these features are natural laboratories for space weathering, an important yet still poorly understood process that affects spectral observations of all airless bodies, such as asteroids and Mercury¹⁰. Another explanation proposed recently is that fine dust, which is widely believed to be lofted above the lunar surface after every terminator crossing^{11,12}, may be accumulating in these regions due to solar wind interactions with the magnetic field¹³. Finally, these bright features are also anti-correlated with surface-bound hydroxyl and water molecules¹⁴. Explanations for this observation are still forthcoming, but the solution will also likely give insight into recently discovered near-surface water on the rest of the Moon¹⁵.

Part of the difficulty in determining the origin of these features is that our measurements have poor spatial resolution, owing to the relatively high altitudes of lunar spacecraft (~20 km). Measurements at the surface, in contrast, would give information about the coherence of the underlying magnetization, addressing whether they formed in a uniform field, as expected from a dynamo. Measurements of the solar wind flux would help test if the solar wind is being kept off the surface by the magnetic field. Measurements of any lofted dust would help quantify how often lofting takes place, and whether it is important in forming swirls.

To accomplish these measurements, one would ideally land on the surface, but the costs of landing are prohibitive. Instead, we have developed a new, leaner concept that calls for sending a cubesat on an unbraked impact trajectory into the hearts of these features. The onboard payload (at minimum, a magnetometer) transmits data to the Earth in real-time, up until the last milliseconds before impact with the lunar surface, enabling first-of-a-kind measurements at < 100 meters altitude (Fig. 3).

Our initial study focuses on the Reiner Gamma swirl. Reiner Gamma's complex surface pattern and strong magnetic fields have made it the prototypical lunar swirl for three decades⁸.

Our primary science objectives at Reiner Gamma are:

1. Constrain the process(es) responsible for magnetizing the underlying material by measuring the structure of near-surface magnetic fields. How complex are the magnetic sources? Is the field structure and direction consistent with material magnetized in a uniform field?
2. Test the hypothesis for formation of the swirl pattern by measuring the correlation of near-surface fields, surface markings, and solar wind flux. Does the magnetic field structure and solar wind flux correlate with the surface pattern? Are vertical near-surface fields associated with the darkest parts of swirls, while horizontal, near-surface fields are associated with the brightest regions, as predicted by the solar wind stand-off model⁹?
3. Use magnetic field and solar wind flux measurements to better understand additional phenomena such as proton reflection¹⁶ and electric fields at swirls^{17,18}.

Secondary objective:

1. Test the hypothesis of lunar dust lofting and its possible role in swirl formation by measuring near-surface lofted dust. What is the distribution of lofted dust grains near the surface (< 1 km altitude)?

Table 1 shows the measurement targets for the magnetometer, solar wind detector, and dust instrument. Because the spacecraft is traveling at approximately 2 km/s at impact, the sampling frequency of each instrument must be high, and it has a strong influence on the measurement resolution.

Table 1. Lunar Impactor measurement targets.

Measurement	Instrument	Measurement target
Magnetic field	Magnetometer (MAG)	200 samples/s (~10 m) of 3-axis magnetic field.
Solar wind	Solar Wind Ion Flux Tracer (SWIFT)	20 samples/s (~100 m) ion energy & angle distribution.
Dust	Lunar Dust sensor (LUD)	20 samples/s (~100 m) dust flux & size distribution. Particle size < 1 μm and original \pm charge state.

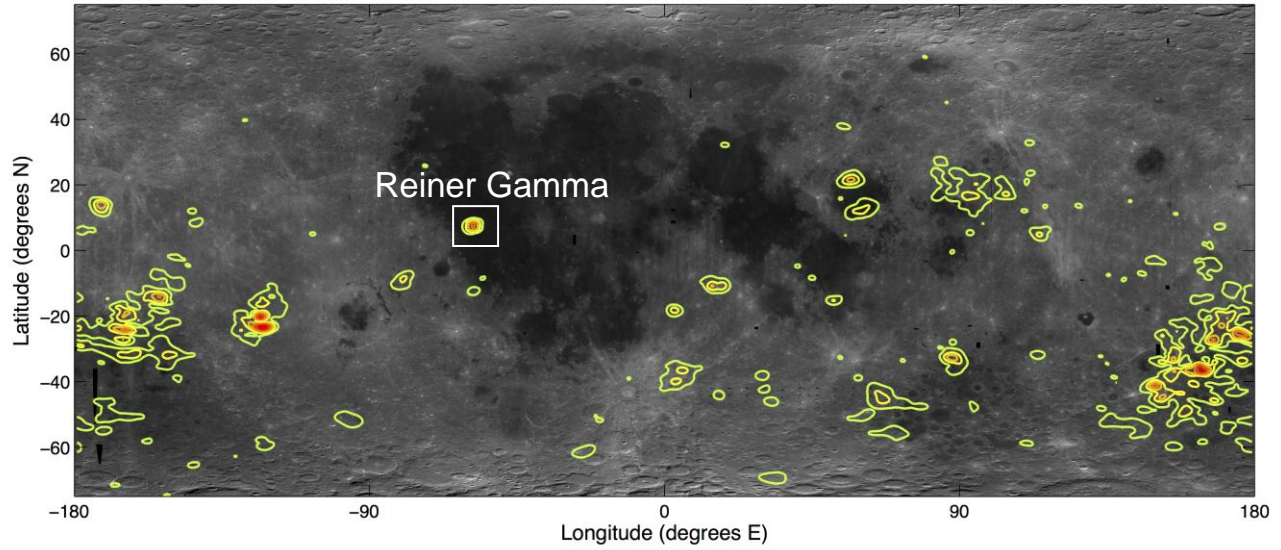


Figure 1. Lunar magnetic field contours over lunar reflectance at 750 nm (near side centered). Contours are 2-12 nT, from the spherical harmonic model of Purucker and Nichols (2010)¹⁹, evaluated at 30 km.

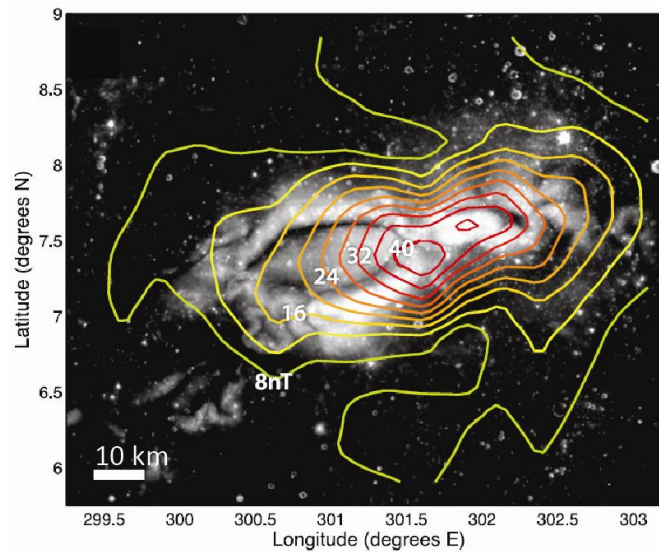


Figure 2. Horizontal component of the magnetic field at Reiner Gamma, using data from individual Lunar Prospector orbits at ~18 km altitude⁹.

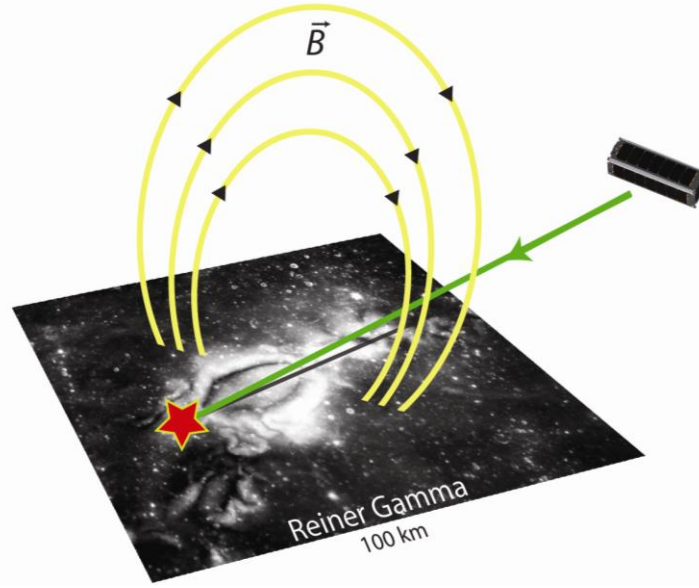


Figure 3. Cubesat on a low-angle impact trajectory into the Reiner Gamma magnetic anomaly.

1.3 Impact angle and trajectory requirements

Previous orbiter missions such as Lunar Prospector and Kaguya have acquired magnetic field data at ~ 20 km altitude, and in limited locations down to ~ 10 km altitude (~ 18 km at Reiner Gamma, Fig. 2). Important information to address the above mission objectives is expected to emerge at sub-10-km altitudes. The impact angle must be carefully chosen to ensure that measurements take place at sufficiently low altitude, over a long enough horizontal distance, to address the objectives. While the lowest possible angle is desired, low angles are more difficult to achieve due to orbital dynamics considerations, especially if the cubesat is not released from a mother-ship. Therefore, defining the minimum impact angle required for mission success is critical. We will focus on the trajectory requirements for the magnetic field and solar wind flux science, and will discuss the requirements on measuring dust in a future study.

At Reiner Gamma, the brightness pattern on the surface exhibits a complex geometry of interwoven bright and dark features, but the magnetic field observed at altitude has almost no such structure. The source model of Hemingway and Garrick-Bethell (2012)⁹ predicts that magnetic fields will exhibit complex structure at altitudes below ~ 3 km, if the solar wind standoff hypothesis is correct. In their model, they assume a 55-dipole source model (with all dipoles having a constant magnetization direction) that produces near-surface vertical magnetic fields at dark interior portions of the swirl (“dark lanes”), and near-surface horizontal magnetic fields (B_h) over bright regions. Figure 4 illustrates a hypothetical ground track designed to traverse two dark lanes at Reiner Gamma, with small red circles illustrating the positions of the dipoles in the source model.

Figure 5 shows profiles of horizontal magnetic field strength predicted at various altitudes above the ground track illustrated in Fig. 4. Figure 5 illustrates how large changes in field structure appear with changes in altitude. The cusp features (where field lines become vertical) in these horizontal field profiles are particularly diagnostic of the overall field structure predicted by the model. If observed, two central cusps co-located with the two central dark lanes would imply that solar wind is reaching the surface in those regions, while adjacent areas are being kept bright due to deflection of the solar wind. Because these two central cusps are not likely observable above ~ 3 km altitude, the spacecraft must pass below this altitude as it crosses the center of the anomaly. We also assume that measurable changes in solar wind flux due to the magnetic field will appear by at least 3 km above the surface (subject to further study).

In cross-section, the magnetic field pattern predicted by the source model (Fig. 4) resembles a simplified line-source model illustrated in Fig. 6. Figure 6 shows that a good impact trajectory would traverse all four cusps and all three peaks in horizontal field strength. The green line in Fig. 6 depicts this path, which we designate as our “goal” trajectory. The purple line depicts the “floor” trajectory, which crosses two of the peaks and three cusps. This trajectory accomplishes

the minimum amount of science for mission success. Finally, the red line represents the lowest altitude reached by the Lunar Prospector spacecraft. Figure 7 illustrates the field directions encountered along the trajectories depicted in Fig. 6.

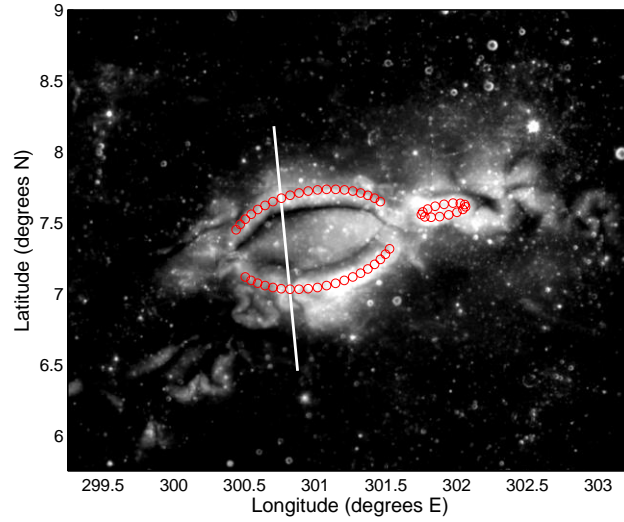


Figure 4. Reiner Gamma overlain with a hypothetical impact trajectory (white) and the source model dipoles from Hemingway and Garrick-Bethell (2010)⁹(red circles).

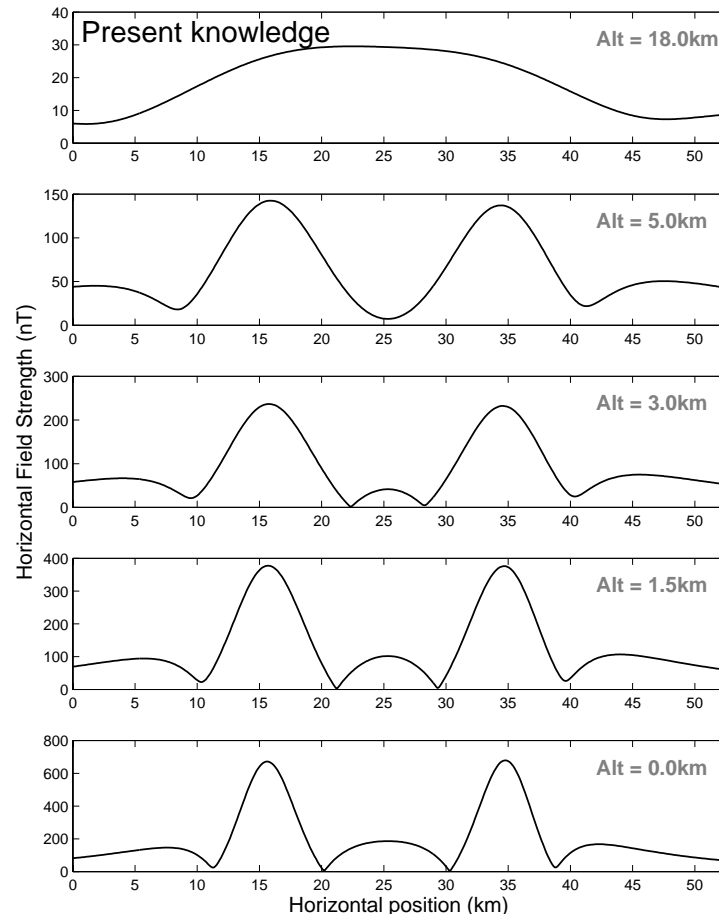


Figure 5. Profiles showing horizontal magnetic field strength predicted at various altitudes, based on the source model. The top panel corresponds approximately to Lunar Prospector's lowest altitude, where fine field structure is not observable.

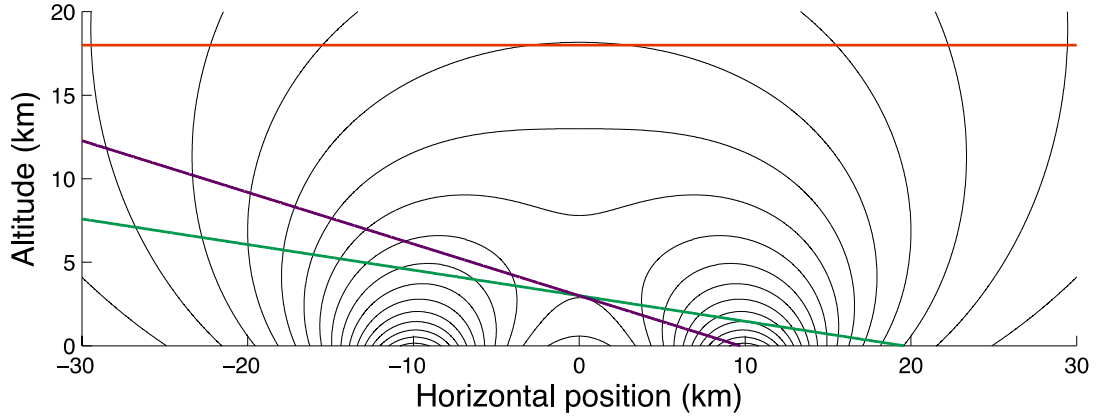


Figure 6. Magnetic field lines for two parallel linear sources magnetized horizontally (a simple analog to the source model in Figs. 4 and 5). The long axis of the sources is perpendicular to their direction of magnetization. The red line represents the lowest altitude reached by Lunar Prospector. The green line represents the “goal” impact trajectory and the purple line represents the “floor” impact trajectory.

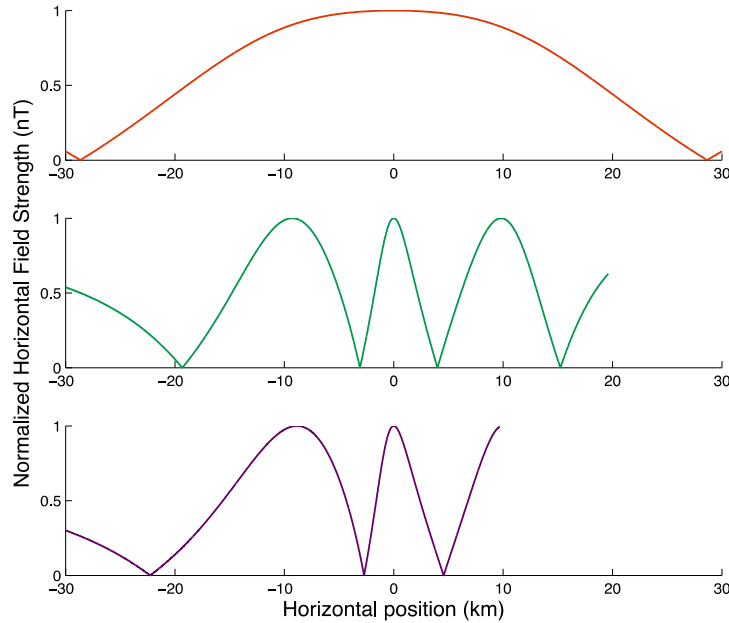


Figure 7. Magnetic field direction along each of the trajectories in Fig. 6. Normalized horizontal field strength is zero when the magnetic field is vertical and unity when the field is horizontal. The red (top) profile represents the field observed by Lunar Prospector and the green (middle) and purple (bottom) profiles represent the field along the proposed “goal” and “floor” trajectories, respectively.

Any uncertainty in the impact position must be accounted for by lowering the required impact angle to ensure that the important features in the field structure can be observed. We can quantify this by the diagram shown in Figure 8. We assume the spacecraft performs useful new measurements below an altitude h , over a horizontal distance $h/\tan\theta$, where θ is the angle the impact trajectory makes with the horizontal. Figure 8 illustrates that uncertainty in the impact position means that the effective ground track distance is given by: $d = h/\tan\theta - \Delta d$, where Δd is the length of the landing ellipse. Here, we assume θ can be perfectly controlled, but this assumption will be revisited in future studies.

In the case of the goal trajectory, in order to observe all four cusps, the spacecraft must traverse a horizontal distance of ~16 km after crossing the center of the albedo anomaly (at which point it must be below an altitude of 3 km in order to traverse the two central cusps). This requires an impact angle of no more than 9.7° , when a 10% margin is added to the desired horizontal distance. However, if the impact position uncertainty is 2 km (distinct from the 10% margin), the

maximum acceptable impact angle is 8.7° . The relationship between impact angle, ground track distance, and impact position uncertainty is illustrated in Figure 9. Table 2 summarizes the required ground track distances and corresponding impact angles assuming impact position uncertainties of zero and 2 km, for the goal and floor cases.

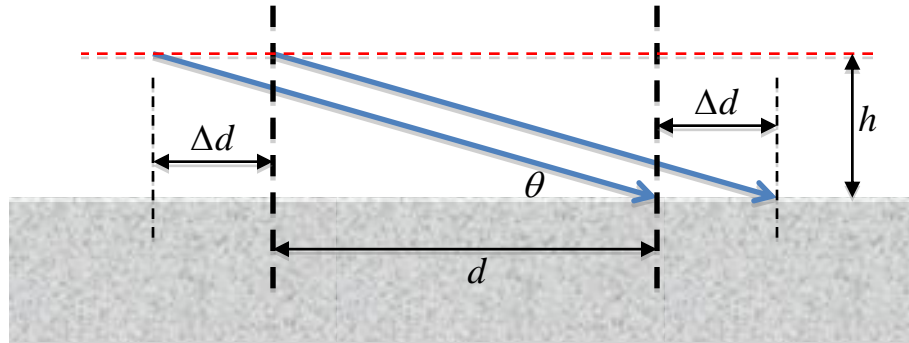


Figure 8. Impact profile showing relationship between impact angle θ , maximum altitude h , landing ellipse length Δd , and useful ground track distance d .

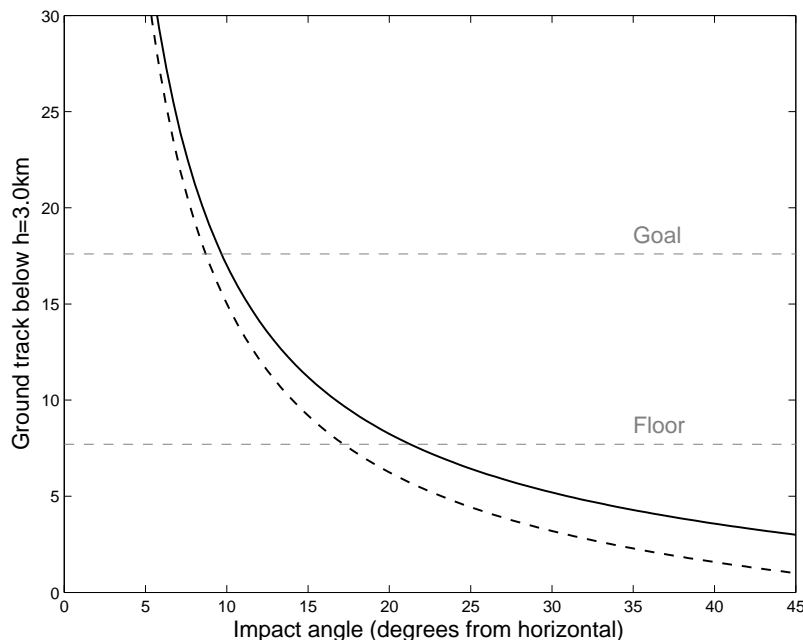


Figure 9. Low-altitude ground track vs. impact angle assuming perfect accuracy ($\Delta d = 0$, solid black line) or a 2-km landing ellipse ($\Delta d = 2$ km, dashed black line).

In summary, to meet the science objectives an impact angle $< 10^\circ$ is strongly desired, but an angle as high as almost 20° would still likely yield important new data. Even if the dipole source model we used to estimate these requirements does not accurately represent the true magnetic field (the model's uncertainty is, of course, the entire reason the mission is needed), measurements below several kilometers altitude at low angles are still likely to produce important new observations that will help address the mission objectives. In the future, we plan to further explore how solar wind flux predictions influence the trajectory requirements, perhaps with simulations¹⁸. In addition, we must assess whether the approach path chosen can be realized by the spacecraft trajectory (Section 7), as well choices of trajectories if multiple Lunar Impactors are built and launched (e.g. for redundancy).

Table 2. Ground track distance (d) and corresponding maximum impact angles (θ) required to achieve science objectives. Ground tracks are assumed to be perpendicular to dark lanes. Minimum required distances are computed according to the predicted separation of peak and cusp features based on the idealized source models in Fig. 6, with 10% margin. The last column accounts for an additional horizontal impact position uncertainty of 2 km.

Objective	Description	d_{\min}	θ_{\max} ($\Delta d = 0$ km)	θ_{\max} ($\Delta d = 2$ km)
Goal	Traverse 4 cusps in B_h	17.6 km	9.7°	8.7°
Floor	Traverse 3 cusps in B_h	7.7 km	21.3°	17.2°

2. INSTRUMENT DESCRIPTIONS

2.1 Introduction

In the next two sections we describe a magnetometer and solar wind sensor for the Lunar Impactor mission. The magnetometer is based on mature flight-tested technology, while the solar wind sensor is a new design based on hardware that will fly on the MAVEN mission to Mars. Dust detector technology will be studied at a later date.

2.2 Magnetometer

The magnetometer will measure the B-field vector in the range 0-200 Hz (Table 1). In traditional space missions this would be achieved using a fluxgate sensor, likely in combination with a search coil sensor (for frequencies above 60 Hz), however, the very low resources available on the cubesat platform (in particular mass and volume) place particular constraints on the instrument design that mean other sensor technologies become attractive. Magneto-resistive sensors (MR) are solid state devices that are less than 1 gram in mass and extremely low volume. Several types of MR sensors exist but it has been shown previously that Anisotropic Magneto-Resistance (AMR) exhibits the best intrinsic detectivity in the DC-100 Hz range due to its superior $1/f$ noise characteristic²⁰. Noise levels can be as low as 30 pT/ $\sqrt{\text{Hz}}$ at 1 Hz, which is competitive with top end fluxgates (<10 pT/ $\sqrt{\text{Hz}}$ at 1 Hz)²¹. In addition, AMR sensors maintain excellent sensitivity with increasing frequency, unlike fluxgates which tends to roll off sharply above 100 Hz.

There exists some flight heritage for AMR magnetometers on small spacecraft. Both the currently active CINEMA missions and Tatiana-2 mission have deployed AMR sensors for applications in the area of space weather measurements^{22, 23}. A design similar to that used on CINEMA is proposed for Lunar Impactor. It is composed of a single electronics card in a standard PC104 form factor. The instrument contains two tri-axial AMR sensors (based on the three single axis HMC1001 sensors from Honeywell Inc.), one triad mounted on the electronics card and the other designed for mounting at a remote location (e.g. on a boom) and connecting to the electronics via a lightweight harness. Fitting of the sensor to the boom is desirable in order to position it away from local field sources on the platform that could contaminate the measurement. A photo of a CINEMA flight model instrument is shown in Fig. 10.

Each single axis AMR sensor is implemented as a full bridge with output voltage varying in response to a change in current flow modulated by the field dependent resistance. The sensors include two straps, one parallel to the sensitive direction (offset strap), and one parallel to the anisotropic direction (set-reset strap). Both straps are used to implement a driven closed loop design in a manner similar to that of a conventional fluxgate, with the exception that the output signal is first as opposed to second harmonic²⁴. In fact, for the CINEMA design it was necessary to combine the drive circuit with the sensor triad in a non-magnetic hybrid circuit in order to minimize the line losses of the driving signal (4 A peak for μs). A photo of the hybrid design realized for CINEMA is shown in Fig. 10, and the instrument parameters are shown in Table 3.

The primary challenges in adapting the current design for Lunar Impactor will be accommodation. We anticipate a boom length of order maximum 15 cm, which will place the sensor much closer to the bus than on CINEMA (where the sensor is 1 m away) from the platform. If a boom is not possible then we may consider arrangements of multiple (at least 2) sensors on the platform which could be used in a differential mode to reject background noise and isolate the lunar signal. Some modification to the electronics is required to increase the cadence from the current 10 vectors/s up to 200 vectors/s. However, this is not expected to be significantly complex, requiring only some modification to the demodulator and associated filter blocks. Ranging is not likely to be required, in the CINEMA design using a 24 bit ADC filtered to 19 bit transmission we achieve 0.25 nT digital resolution in a single $\pm 55,000$ nT range, which will be more than enough for lunar field studies (maximum field range of $\pm 10,000$ nT will be easily sufficient). Radiation

susceptibility of the externally mounted sensors is not anticipated to be a problem, as the HMC1001 sensors do not show significant degradation of sensitivity in radiation dose testing²⁵.

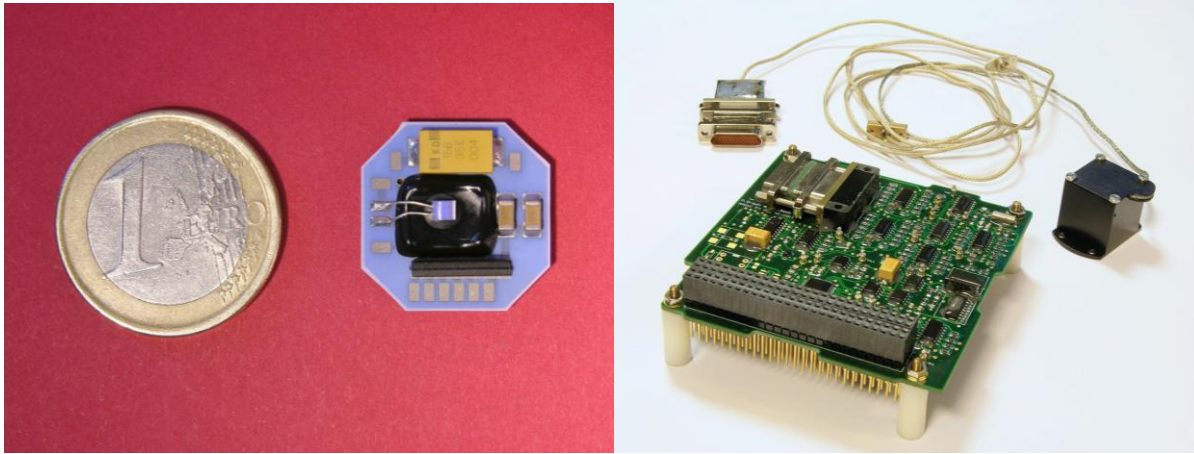


Figure 10. Left: Photo of the hybrid magnetoresistive sensor. Right: Photo of the CINEMA magnetometer (MAGIC). It is composed of PC104 card and hybrid sensor connected by a 1 m harness.

The CINEMA design has been launched once to date in 2012. The same design will see two more launches in 2013 and a modified design will launch on the NASA Sunjammer mission in 2014. It is anticipated the Sunjammer magnetometer electronics design could be implemented in FPGA, depending on schedule, which would be timely for Lunar Impactor as it will reduce the footprint required on the cubesat platform to an area less than half the size of the current PC104 card.

Table 3. Key parameters of the Lunar Impactor magnetometer (derived from CINEMA design).

Property	Value
Mass	0.12 kg
Power	400 mW (science mode)
Volume	Sensor head 10 cm ³ , Electronics 173 cm ³ (9 cm x 9.6 cm x 2 cm)
Sensitivity	<2 nT
Cadence	1 vector/s (HK mode), 200 vectors/s (science mode)
Telemetry	<2.5 kbits per second
Noise Density	50 pT/√Hz at 1 Hz
Temperature	-50° C to +60° C

2.3 SWIFT (Solar Wind Ion Flux Tracer)

The SWIFT instrument is designed to track the deflection and deceleration of incoming solar wind ions at low altitudes within lunar crustal magnetic fields. The measurement requirements for a solar wind sensor for Lunar Impactor are stringent. An optimal sensor must cover a large portion of one hemisphere, with an energy range from fast solar wind down to highly decelerated solar wind (with good energy resolution over this range). It must also make measurements with a very high cadence in order to trace the spatial structure of the deflected solar wind ion fluxes inside the magnetic anomaly region at sub-km scales, while the measurement platform skims through the anomaly at ~2 km/s. Finally, it must also do all of this with the very low resources available for a cubesat-style payload.

SWIFT provides a sensor optimized for this task. The SWIFT sensor measures reduced ion distribution functions as a function of two orthogonal velocity components extremely rapidly; these can then be de-convolved to provide a 2-dimensional map of ion flux for each energy step. To accomplish this, SWIFT utilizes a single hemispherical electrostatic analyzer with two crossed apertures, each with a 120° x 10° instantaneous field of view, with electrostatic deflection to cover all angles in a 120° x 120° field of view. By sweeping the voltage on the inner hemisphere logarithmically, and sweeping the voltage on the two deflectors at each energy step, we can cover all angles for ions with

energies from 100 eV to 2 keV in as fast as 50 ms (20 Hz). The instrument also has a solar wind tracking mode, which provides better time resolution, at the expense of a reduced angular field of view and energy coverage (centered on the solar wind peak).

The electrostatic analyzer for SWIFT utilizes a full hemisphere design rather than the top-hat more typically used for a less resource-constrained instrument, allowing a single detector to accept particles over a much larger angular range ($120^\circ \times 10^\circ$). This naturally reduces the intrinsic angular resolution (in effect, the sensor measures a distribution reduced in one velocity dimension); however, by utilizing two detectors with perpendicular fields of view (Fig. 11), we can deconvolve the full ion distribution.

Table 4. Key parameters of the Lunar Impactor SWIFT instrument.

Capability	Lunar Impactor Requirement	SWIFT performance
Energy Range	100 eV – 2 keV	Intrinsic 10 eV – 5 keV Fast Sweep 100 eV – 2 keV
Energy Resolution	33%	Intrinsic 15% Fast Sweep 33%
Measurement Cadence	20 Hz (100 m scale)	Fast Sweep 20 Hz SW Tracking 200 Hz
FOV	$90^\circ \times 90^\circ$	$2 \times 120^\circ \times 120^\circ$ Crossed FOVs
Angular Resolution	$20^\circ \times 20^\circ$	$10^\circ \times 10^\circ$

The analyzer is in part based on a similar instrument flown on ISEE-3 in 1980, and the associated electronics have been successfully flown by UCB on the ISEE-3, Wind, FAST, THEMIS missions (and currently in use on the MAVEN STATIC and SWIA instruments (Fig. 12), now in spacecraft level environmental testing). By utilizing a hemispherical analyzer instead of a more typical top-hat, we can measure a large portion of 2π with only two small channel electron multiplier detectors and two electronics chains. This stands in contrast to a top-hat, which would require a heavy stack of microchannel plates (MCP), and sixteen power-hungry electronics chains to achieve the same measurement. The high voltage supplies are much the same as those used by a top-hat, and are easily achievable in a few small boards, especially since there is no need to go to high energies of more than a few keV for this application. The digital board utilizes only straightforward processing capability to control the preamps and the high voltage sweeps, sample basic housekeeping, process two counter inputs, and communicate with the spacecraft via a serial interface. All of the electrical designs, including HV and digital processing make heavy use of high-heritage designs developed over many years and flown on Wind, FAST, THEMIS, MAVEN. A block diagram is shown in Fig. 12.

The end product is a high-resolution measurement of ion fluxes both within and outside the anomaly region, allowing us to trace how solar wind ions are decelerated and deflected by the complex magnetic and electric fields inside the anomaly region. Ultimately, this will allow us to understand how the presence of the magnetic anomaly may affect surface weathering beneath it, and whether this can explain the enigmatic lunar swirls.

SWIFT provides an optimal instrument for the Lunar Skimmer mission, providing rapid 20 Hz measurements of solar wind ions over a large field of view. A similar sensor would also be of interest for almost any mission wishing to make fast measurements of a high flux of ions like that from the solar wind. Additionally, SWIFT provides a sensor that is more intrinsically radiation-tolerant than a top-hat, since it uses channel electron multipliers rather than MCPs, and therefore may also be of interest for missions with a high radiation dose.

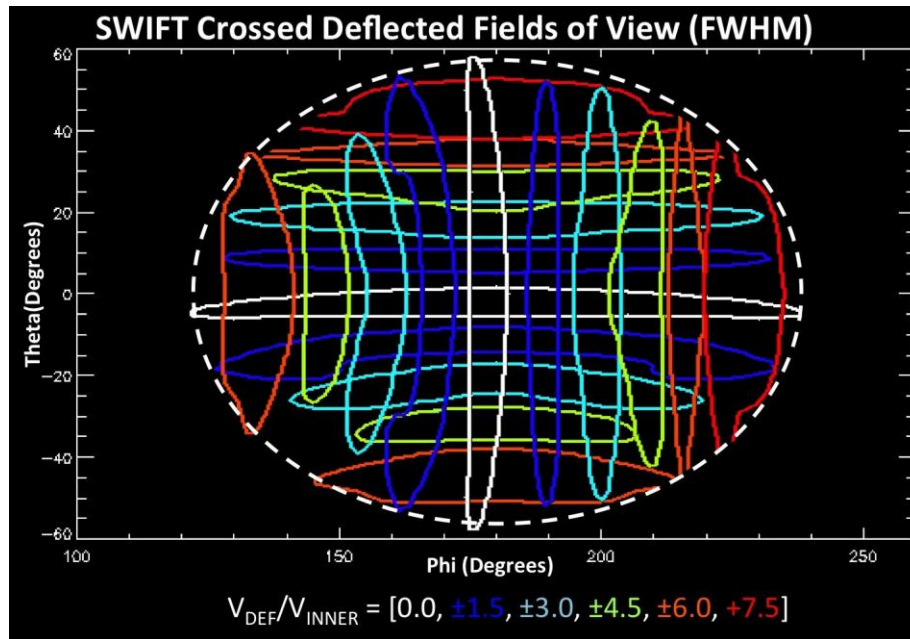


Figure 11. Electrostatic optics simulation of the SWIFT instrument, showing the full-width at half maximum for the response of each of the two crossed fields of view, for each deflection angle, at a given energy step. By processing the count rates accumulated in each of these instantaneous fields-of-view, the solar wind ion distribution can be de-convolved with high accuracy over the entire $120^\circ \times 120^\circ$ field of view.

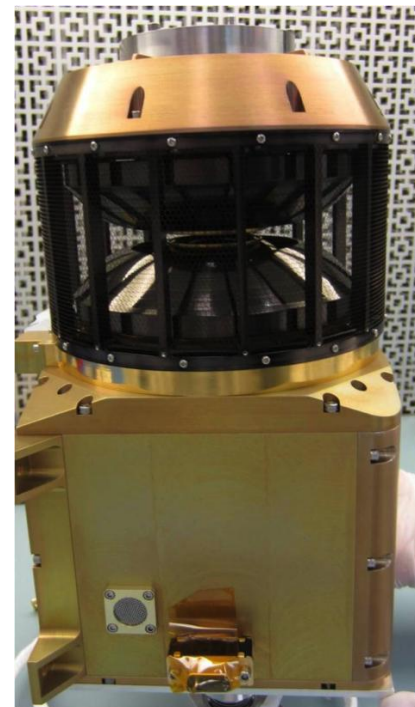
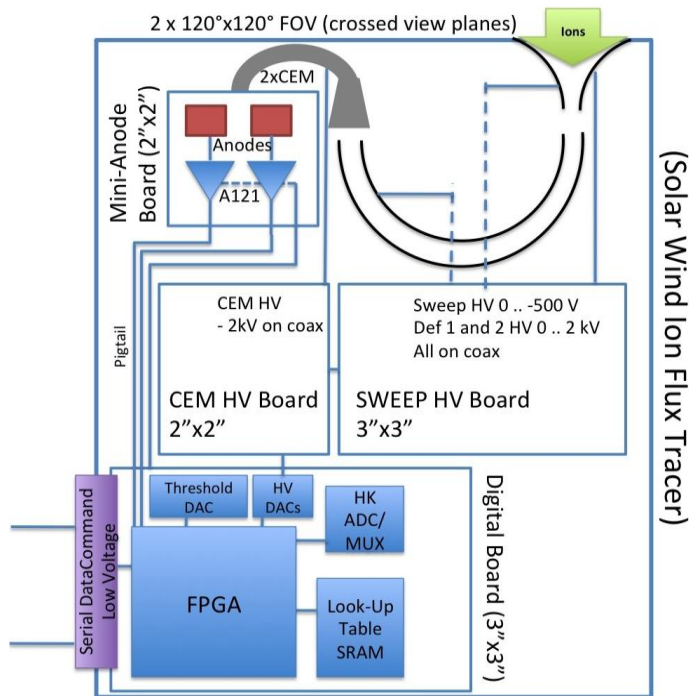


Figure 12. Left: A simplified electronic block diagram for the SWIFT instrument. Right: The Solar Wind Ion Analyzer for the MAVEN mission, which provides most of the heritage electronics for SWIFT (though in a more massive package).

3. MISSION ARCHITECTURE 1 – MOTHER-SHIP WITH CUBESAT DAUGHTERS

3.1 Planetary Hitchhiker

As discussed in the Introduction, we will review two mission architectures to deliver the Lunar Impactor cubesat on a trajectory with the surface. First, we discuss an architecture that releases the cubesats from a mother-ship in lunar orbit. To keep the cost of this architecture low, the mother-ship has been designed to be small enough to share a ride to geostationary orbit (GTO) before making its way to the Moon. This mother-ship is therefore known as Planetary Hitchhiker (PHH).

One of the major advantages of the PHH design is its compatibility with a variety of launch vehicles as a secondary payload accommodation. Preeminent amongst those is the EELV Secondary Payload Adapter (ESPA) standard, which can accommodate a 181 kg, 96 x 71 x 61 cm spacecraft. The current PHH concept at 96 kg (wet mass) and 86 x 65 x 44 cm is well within this envelope. In the nominal ESPA mission profile, the primary payload, which sits atop the ESPA ring, separates at its intended injection orbit (herein assumed to be GTO). The EELV upper stage then performs a series of orbital maneuvers in order to release up to six ESPA payloads at their proscribed initial orbits. Alternatively, an innovative cost effective option involves packaging PHH within the spare battery compartment of a series 1300 Loral communication satellite. This option is currently being studied further.

After PHH is placed into GTO by the launch vehicle, three apogee-raising burns totaling 800 m/s are performed by its chemical propulsion system. Next, a burn must be performed to target the weak stability boundary (WSB) to put PHH on a near-lunar trajectory, after which Lunar Orbit Insertion (LOI) takes place (Fig. 13). The WSB trajectory gives PHH the flexibility to reach the Moon from any GTO orientation (with varying time) and requires less Δv , allowing for a range of launch opportunities. Once in lunar orbit, station-keeping, orbital repositioning for nanosatellite impactor release, and a deorbit burn will be performed using the propulsion system. The deorbit burn will take place at the end of useful mission, near the end of propellant life, when the spacecraft will be maneuvered into a descent trajectory for impact on the lunar surface. During the de-orbit descent, PHH can provide an additional opportunity for scientific measurements.

The PHH spacecraft contains a 6U cubesat dispenser that hosts the impactors, and accommodates any payload that conforms to the published Cubesat Design Specification. The PHH spacecraft is comprised primarily of space-rated, radiation-hardened parts (per GSFC EEE-INST-002) with components, assembled into a custom bus architecture. The bus is 3-axis-stabilized with 1300 m/s of propulsion.

The avionics unit is a flight-proven design and is inherited from both the LCROSS and LADEE missions. Flight software leverages LADEE heritage (with common-code reuse), using GSFC CFE/CFS as the core program. The software STK and ODTK will be adopted for ground-based orbit determination. Three reaction wheels and an accelerometer supplement the six attitude control system (ACS) thrusters for attitude control. Four coarse sun sensors and a star tracker comprise the ACS sensor suite. Dual-frequency S-band helix antennas on the bus provide communication with the Ames multi-mission operation center and deployable UHF antennas on the impactors allow them to communicate with the mother-ship.

The PHH spacecraft has body-mounted solar panels (104 W capacity) to power a 24 A-h battery in addition to providing structural support. Multi-layer insulation and surface coatings, along with several patch heaters, will be used for spacecraft thermal control.

Excess tank capacity supports an additional 300 m/s Δv , above the required 1300 m/s Δv . A >6 dB link margin is available at all phases using an 11 m antenna at UC Berkeley. The UHF crosslink between each cubesat impactor and the spacecraft is 20 kbps and the downlink of science data from the spacecraft in lunar orbit to ground is 5.5 kbps. Figure 14 shows a drawing of the spacecraft, and Table 5 lists some of its properties.

Extensive lunar orbit modeling accounting for gravity perturbations was completed to validate the concept of operations and maneuvers requiring minimal propulsive station keeping (highlights in Fig. 13). However, a detailed navigation and attitude control error budget still must be assessed. Electrical interfaces and detailed ejection operations between the Loral satellite and PHH must be defined before the battery compartment can be considered a viable launch option.

Finally, in order to keep spacecraft mass and launch cost low, a high density I_{sp} monopropellant is required. Many monopropellants have been studied in preparing the PHH design, but those with the highest performance typically require higher development. Technology maturation of a high performance monopropellant is required in order to enable the PHH mission without increasing complexity or mass.

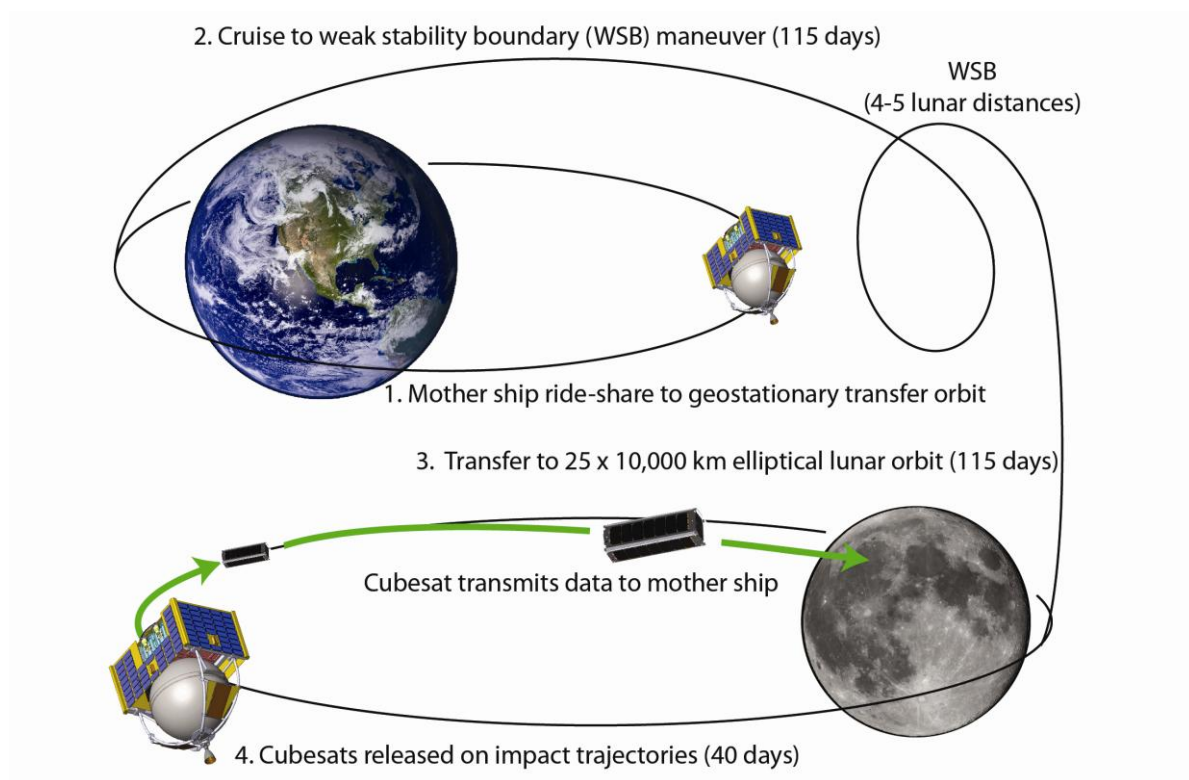


Figure 13. Mother-ship architecture with the Planetary Hitchhiker spacecraft.

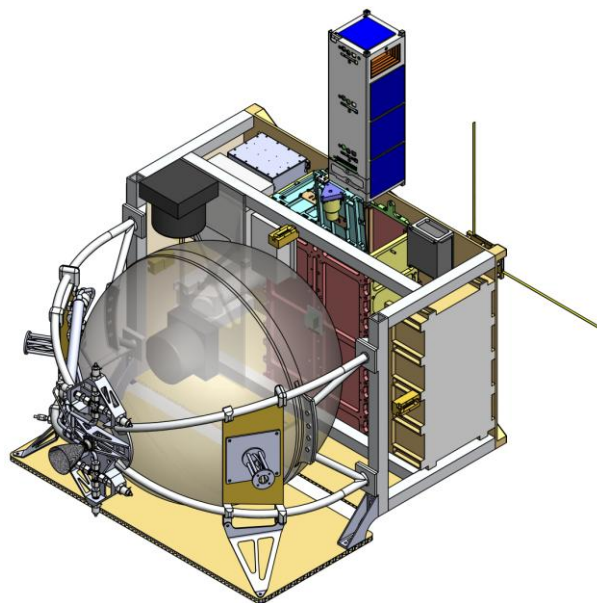


Figure 14. Planetary Hitchhiker releasing one of two cubesat impactors.

Table 5. Planetary Hitchhiker properties.

Property	Current Estimate	Maximum Possible	Margin
Total Mass	96 kg	181 kg	88%
Solar Power	75 W (Maximum)	98 W (End-of-Life)	>31%
Battery Power	193 Wh	691 Wh	258% (28% DOD)
Propellant	28 kg	36 kg	33%
Downlink Data Rate	2 kbps	5.5 kbps	175%

4. MISSION ARCHITECTURE 2 – CUBESAT-ONLY APPROACH

4.1 Overview of the cubesat-only approach

Below we describe an architecture where the cubesat transfer to the Moon from Earth-orbit using an ion electrospray propulsion system instead of a mother-ship. Besides the communication, navigation, and propulsion challenges that we discuss, radiation exposure in this architecture is a concern. Because most cubesat hardware is not presently capable of tolerating large radiation doses, we assume that the starting orbit is GEO, or in a lissajous orbit about the Earth-Sun L1 point. While more expensive than a ride share to GTO, starting in GEO avoids passage through the most intense portions of the radiation belts. The L1 starting point has even less radiation exposure, but there are fewer launch opportunities to L1. As described above, starting from GEO could be realized by a ride share in the spare battery compartment of a Loral 1300 series communication satellite. Therefore, the most promising option is starting from GEO, and most of the following analysis focuses on this mission profile (Fig. 15).

Design concerns such as the flight computer, power processing system, sun sensors, and other hardware, will be presented elsewhere. However, the mass and volume of all components is expected to permit at least the magnetometer to fly as a payload.

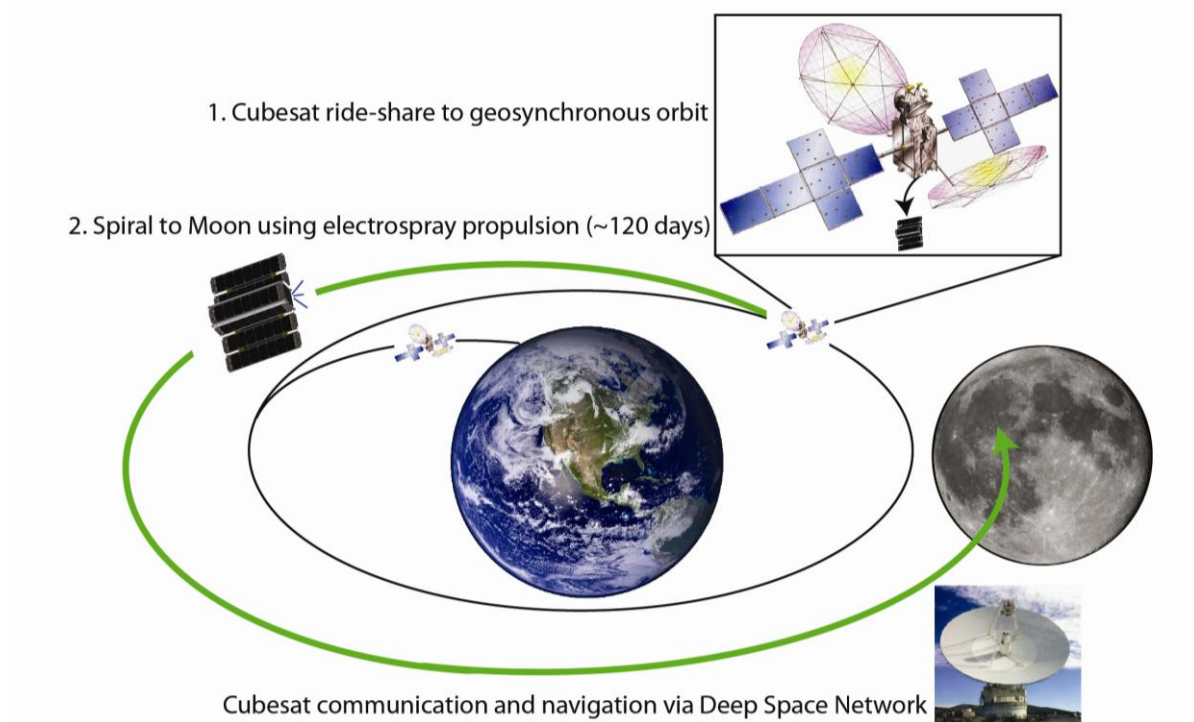


Figure 15. Cubesat-only approach starting from geosynchronous orbit.

5. COMMUNICATION AND NAVIGATION – CUBESAT-ONLY APPROACH

5.1 Cubesat hardware

For the cubesat transponder and radio, we assume a digital version of the LMRSat mission radio that is now in development²⁶. The package is expected to occupy a volume of approximately 0.5U.

5.2 Concept of operations

Mission, science and navigation operations for Lunar Impactor are carried out at Space Sciences Laboratory (SSL) at the University of California, Berkeley (UCB). Lunar Impactor operations are based on UCB's experience with the Acceleration, Reconnection, Turbulence and Electrodynamics of the Moon's Interaction with the Sun (ARTEMIS) mission. ARTEMIS is an extension of the Time History of Events and Macroscale Interactions during Substorms (THEMIS) mission – a 5-spacecraft constellation launched in 2007²⁷. When the primary THEMIS mission was completed in 2009, two of the five spacecraft were maneuvered from Earth to lunar orbits, using a low-energy transfer trajectory with multiple Earth and lunar gravity assists. As part of this journey, the two spacecraft operated in Earth-Moon libration orbits (LL1 and LL2) for approximately 9 months prior to insertion into stable lunar orbits in 2011^{28, 29}.

5.3 Communications scenarios and assumptions

The THEMIS/ARTEMIS probes carry coherent S-band ranging transponders that are similar to the Lunar Impactor communications system (except for the frequency band), and were originally designed to operate in Earth orbits with 9-13 m class ground stations, and primarily with the Berkeley Ground Station (BGS) 11-m antenna. For the ARTEMIS mission extension, the required ranges for communications increased from 200,000 km up to 1,600,000 km for some of the trajectory regimes. Therefore, the 34-m subnet of NASA's Deep Space Network (DSN) was brought online and certified³⁰ to support telemetry reception, command transmission, as well as two-way Doppler tracking and ranging.

One of the ranging techniques that DSN employs is sequential ranging, involving transmission of sequences of periodic ranging signals that are coherently related to each other and to the uplink carrier frequency³¹. The basis of this scheme is a well-defined table of so-called range components that are numbered 4 through 24 with increasing periods.

For ARTEMIS, the available bandwidth in the ranging channel is 384 kHz, allowing range component numbers 6-20 to be used. The resulting one-way range ambiguity resolving power is approximately 9,572 km. Range cycles are 131 s long, with integration times of 30 s for the clock component (number 6), and 6 s for each of the ambiguity resolving components (numbers 7-20). With this scheme, a ranging power-to-noise spectral density ratio of 20-30 dB-Hz was achieved with ARTEMIS at ranges of the order 1,000,000 km.

Future BGS upgrades to allow for telemetry reception in the Space Research Service (SRS) X-band segment (8450-8500 MHz) and for command transmission in the 7190-7235 MHz band, in addition to S-band are under consideration. These upgrades comprise installation of a dichroic subreflector, an X-band feed, a diplexer, down and up-converters, and a transmit power amplifier at the Cassegrain focus to allow for S-band transmit/receive and X-band transmit/receive operation. The 11-m primary reflector already has all necessary cut-outs and bolt patterns at the apex to allow for this upgrade, as X-band capabilities were already envisioned to be installed at a later time when the system was manufactured. Design, implementation, testing and certification of this X-band upgrade are performed with in-house expertise and resources at SSL and a small amount of contractor support.

5.4 Link calculations

The cubesat carries an X-band ranging transponder for communications with the ground. On the spacecraft side, a transmit power of 2 W and an antenna gain of 4 dBic is assumed. A link analysis was performed for three scenarios: a high and low data rate case for communicating via the DSN 34-m subnet, and a low data rate case for BGS. Relevant performance data for the DSN 34-m Beam Waveguide (BWG) antennas were taken from Kinman (2009)³¹, and those for BGS are based on data from similar systems. Results for two of the three cases are summarized in Table 6.

With DSN, the telemetry and command links are closed at a range of 410,000 km and a telemetry information rate of 64 kbps with a link margin of 10.8 dB. If a low-energy trajectory is chosen that carries the spacecraft out to the Sun-Earth L1 region at a range of 1,600,000 km, then the telemetry link is still closed at an information rate of 4 kbps with a margin of 11.0 dB. An 11-m class antenna such as BGS can close the telemetry link at an information rate of 4 kbps out to lunar distances. For commanding, an information rate of 1 kbps is selected, providing link closure in all cases.

Extrapolating from the experience with ARTEMIS, the DSN 34-m subnet stations should have a sufficient carrier to noise ratio in the ranging channel to lock up on the sequential range data out to the L1 region.

Table 6. Link analysis for two different ground stations.

Parameter	DSN 34-m BWG Antenna	BGS 11-m Antenna
Frequency [MHz]	8450.0	8450.0
Spacecraft Transmit Power [W]	2.0	2.0
Spacecraft Passive Losses [dB]	1.5	1.5
Spacecraft Antenna Gain [dBic]	4.0	4.0
Spacecraft EIRP [dBW]	5.5	5.5
Range [km]	410,000	410,000
Free Space Path Loss [dB]	223.3	223.3
Polarization Losses [dB]	0.5	0.5
Pointing Losses [dB]	0.5	0.5
Ground Antenna Size [m]	34.0	11.0
Ground Antenna Efficiency [%]	87.0	55.0
Ground Antenna Gain [dBic]	68.3	56.5
Ground Component Losses [dB]	0.05	0.3
Receiver System Noise Temp. [K]	21.0	98.7
Ground Receiver G/T [dB/K]	55.1	36.6
Modulation Type	PCM/PSK/PM	PCM/PSK/PM
Modulation Deviation [rad]	1.5	1.5
Modulation Loss [dB]	2.1	2.1
Required Bit Error Rate	1.0e-6	1.0e-6
Coding Gain* [dB]	8.0	8.0
Information Rate [kbps]	64.0	4.0
Required Eb/No [dB]	2.5	2.5
Predicted C/No [dB-Hz]	65.0	46.4
Predicted Eb/No [dB]	14.8	8.4
Implementation Loss [dB]	1.5	1.5
Predicted Link Margin [dB]	10.8	4.4

* Concatenated rate-1/2 convolutional (K=7) and Reed-Solomon (223,255,I=5) coding.

5.5 Orbit determination

Orbit determination will use the Orbit Determination Toolkit (ODTK) software by Analytical Graphics Inc. with two-way Doppler and range measurements from DSN, and two-way Doppler measurements from the Berkeley Ground Station. With the use of back orbit data, achieved thrust performance will be reconstructed and input into the force modeling process, allowing the orbit determination system to account for the accelerations generated by the spacecraft's continuous maneuvering.

Based on experience from ARTEMIS, it is estimated that during the cruise phase from the Earth to the Moon, at least 2-3 tracks per day with durations of at least 2-3 hours are required to collect a sufficient number of range and range rate observations. Tracks from ground stations in both the northern and southern hemisphere will be required. The DSN complex in Canberra, Australia will likely need to support half of the tracks, while the other half can be split between the DSN complexes at Goldstone, California, and Madrid, Spain. Additional BGS tracks may provide range rate observations.

5.6 Discussion of trades, complexities and challenges

Future work includes development of more detailed scenarios to determine the achievable navigation accuracy as a function of thrust performance, attitude stability, as well as number and duration of ground station tracks. Most of the operations related complexities will arise from the fact that thrusting needs to be taken into account for the orbit determination process. Given the high level of DSN resource contention, it will also be difficult to find sufficient tracking time to support Lunar Impactor navigation operations with the required accuracy.

5.7 Qualitative assessment of results

It will be challenging to determine the mission trajectories with the required accuracy in the presence of quasi-continuous thrusting, as it depends on the stability of both the thrust performance and the attitude control system. For conventional orbit determination, the trajectory arcs are divided into thrust and thrust-free sections. For Lunar Impactor this will not be possible, so accurate force modeling needs to be included in the differential correction process for orbit determination. The concept of operations will need to allow for navigation planning and data processing in a forward rolling manner. Experience and lessons learned from NASA's Dawn mission that featured quasi-continuous thrusting with an ion propulsion system should be applicable to Lunar Impactor.

6. PROPULSION SYSTEM – CUBESAT-ONLY APPROACH

6.1 Propulsion system background

Ion electrospray propulsion is based on the electrostatic extraction and acceleration of positive and negative ions from an ionic liquid, a zero-vapor pressure conductive salt that remains in the liquid phase at room temperature³² (Table 7). Electric fields on the order of 1 V/nm are required to extract charged species. Such intense fields are routinely achieved at the tip of electrically stressed liquid menisci or Taylor Cones, which form most readily at the end of sharp emitter structures where the electric field intensity is magnified. Emission occurs from the tip of the Taylor Cone; the ions are accelerated and pass through a downstream extractor aperture (Fig. 16).

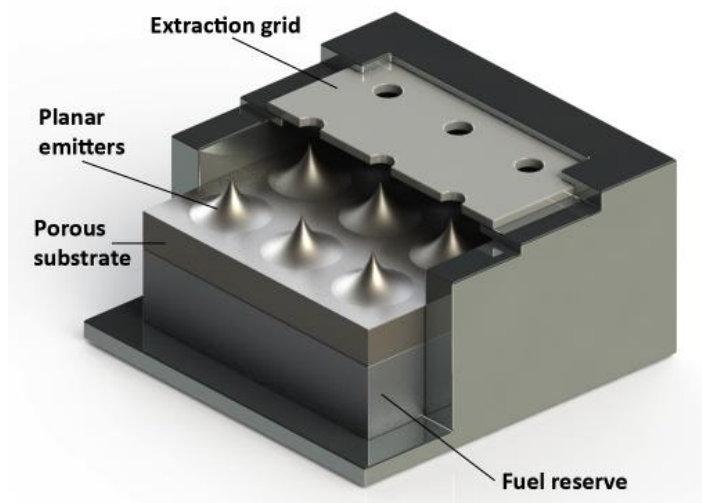


Figure 16. Ionic liquid propellant is transported by capillary action into a porous substrate and ions are extracted from multiple emitters.

Each emitter is capable of generating up to 1 μA of ionic current, corresponding to about 0.1 μN of thrust. The thrust obtainable from single electrospray emitters is too small for most practical applications. Because of this, there is a need to build dense arrays of emitters that fire in parallel. This is achieved by merging the fundamental working principles behind ion electrospray thrusters with recent developments in Micro Electro Mechanical Systems (MEMS) materials and processes (Fig. 17). Emitters are fabricated on porous materials so that propellant can flow via capillarity through the

bulk of the material, driven by the ion evaporation process (Fig. 16). Therefore, no pressurization is required for pumping (or storing) the propellant. The MIT Space Propulsion Lab has demonstrated arrays that achieve high specific impulse ($I_{sp} > 2000$ s) at high efficiency ($\eta > 0.8$) in an extraordinarily compact package^{33, 34}.

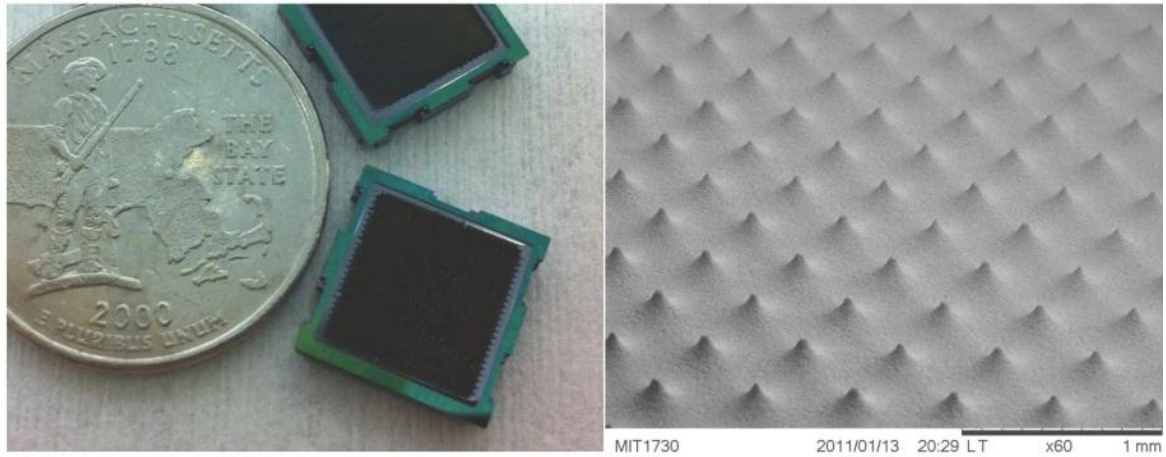


Figure 17. Ion electro spray propulsion system thruster array and electron microscope image of porous nickel micro-tips.

Another characteristic of ion electrosprays is that both positive and negative species can be emitted. In consequence, there is no need for an electron-neutralizing cathode. In a practical configuration, the thruster module includes two separate head modules emitting oppositely charged ions of comparable mass and producing similar thrust. Chemical stability of the propellant is achieved by periodically alternating the polarity of modules or groups of modules, each having its own ionic liquid reservoir. This strategy was identified early in the development of ionic liquid ion sources to avoid electrochemical degradation³².

These ion electro spray thruster arrays are designed specifically for small spacecraft applications and are ideally suited for the Lunar Impactor mission. The simplicity of the propellant feed system coupled with the high density of ionic liquids ensures that the flight assembly will be compact. Work on the power processing unit is progressing steadily, promising high efficiency and low mass and volume. This cutting edge technology brings ambitious missions such as this into the realm of practicality.

Table 7. Ionic liquid properties.

Ionic liquid	Conductivity (Si/m)	Viscosity (cP)	Surface Tension (dyn/cm)	Density (g/cm ³)	+ ion mass (amu)	- ion mass (amu)	E-chem window (V)	Melting point (°C)	Decomp. temp (°C)
EMI-Im	0.84	28 (25 °C)	41.6	1.52	111.2	280.1	4.1	-15	450
EMI-BF4	1.3 (25 °C)	34.1 (25 °C)	52	1.24	111.2	86.8	4.5	12	412
	2.3 (50 °C)	15.6 (50 °C)							
	4.6 (100 °C)	4.7 (100 °C)							

6.2 Design requirements, challenges, and thruster configurations

There are several key challenges in designing the propulsion system. First is thruster lifetime; this mission requires 1800-2200 hours of firing. The MIT Space Propulsion Lab (SPL) is conducting an aggressive testing campaign to evaluate long duration performance. Mitigation of limiting factors like electrochemical degradation and emitter fabrication is underway. A second challenge is redundancy. The spacecraft must be able to maintain its course if it suffers module failures. Since the modules occupy so little volume, it is possible to include extra modules with minimal difficulty. Third is attitude control. The thrusters must be configured in such a way that they provide full three-axis control, and they must be able to compensate for perturbations. Additionally, the power processing unit must be able to provide the necessary number of channels to drive attitude control modules or groups of modules separately. Fourth is

radiation mitigation. Starting in GEO reduces radiation belt concerns, but the electronics, particularly the power processing unit (PPU), must be able to survive the cis-lunar environment. A radiation-hardened version of the PPU is under study and key components of the Precision Electrospray Thruster Assembly (PETA) unit discussed below can be procured in hardened versions. Fifth is sizing; mass and volume are severely constrained in a 3U cubesat. The high density of ionic liquids and the simplicity of the propellant feed and storage system offer unparalleled performance. Optimization of specific impulse, propellant mass, and other properties will occur when the mass of the payload and bus are more fully defined. A 10% Δv margin will be included to account for unplanned course and attitude corrections.

Thruster geometry is a major design consideration. The propulsion system must be compact, easy to integrate with the rest of the bus, and provide adequate forces and torques for three-axis control. An example from which the Lunar Impactor propulsion system can be derived is the PETA unit built for the iEPS thrusters under a NASA Phase II SBIR with Espace Inc. in collaboration with MIT SPL. The PETA PPU boards are designed to fit within a cubesat format to facilitate their testing and operations on the small platforms.

The cubesat-sized PETA engineering model (EM) PPU is shown in the left of Fig. 18, with one thruster-pair and its associated tanks (each ~1 cc in volume) on the far right corner of the board. This PETA unit has two-boards and supports two channels (to switch on or off two independent groups of thrusters). The locations for seven more thruster pairs are outlined on the board. The unit has a mass of 125 g when integrated with four thruster pairs and loaded propellant tanks. Each thruster pair can be configured to either thrust normal to the board, or laterally.

Shown on the right side of Fig. 18 is a three-board/six-channel PETA prototype model (PM) PPU that can provide pitch, yaw, roll and thrust control with 8 thruster pairs (16 thruster modules and tanks). The PPU power requirement depends on the commanded thrust level, and is limited to about 5 W, to fit within reasonable cubesat power budgets. The thruster assembly with a total of about 20 g of propellant provides a total of 200 m/s to a 3 kg nanosat.

The Lunar Impactor baseline requirements differ in terms of propellant mass (~400 g, Section 7) and maximum power budget (~30 W). Fortunately, the current high-voltage board design is scalable and can be upgraded to 30 W using COTS components up-rated for higher power operations with lay-out modifications to accommodate part foot-prints and the higher currents and heat dissipation, which is minimized by a high conversion efficiency. The required total tank volume is about 330 cc (~0.3U).

To provide attitude control on Lunar Impactor, a four-channel two-board configuration using the two “bottom” PETA PM boards independently driving four lateral micro-thruster pairs (with tanks) can provide pitch, yaw and roll authority. Four independent lateral thruster pairs can be configured, for example, on one diagonal of the engineering model board shown in Fig. 18 to provide pure “roll” torque, and pitch / yaw authorities (with some linear thrust). (Another possible thruster configuration with similar capabilities using some “normal” thruster pairs is shown in the notional Fig 19.) A higher power board, coupled with a switch/thruster-tank interface board can separately handle the higher thrust primary propulsion. The attitude control and primary propulsion assemblies can be separated on the platform. Primary propulsion is provided by a separate cluster of thruster modules mounted on the base panel, and these are all serviced by two larger propellant tanks (to enable positive and negative polarities to be fired at the same time). As many arrays will be mounted on the base as possible, since this would minimize the current flowing through each individual thruster, thereby minimizing wear and also permitting thruster failures. Current prototype modules have a thrust density of 25 $\mu\text{N}/\text{cm}^2$, meaning 64 cm^2 of area (32 modules) is required to achieve the desired thrust of approximately 1-2 mN (Section 7). The available area on the base is approximately 80 cm^2 , such that 8 extra modules can be included for redundancy. Thrust density is expected to double or triple in subsequent thruster models, meaning redundancy can be greatly increased. This configuration minimizes complexity as well as volume. As a whole, the derived four-board and thruster-tank configuration providing attitude control and primary propulsion would occupy a total of ~750 cc, or ~3/4U, with a mass of ~ 650 g.

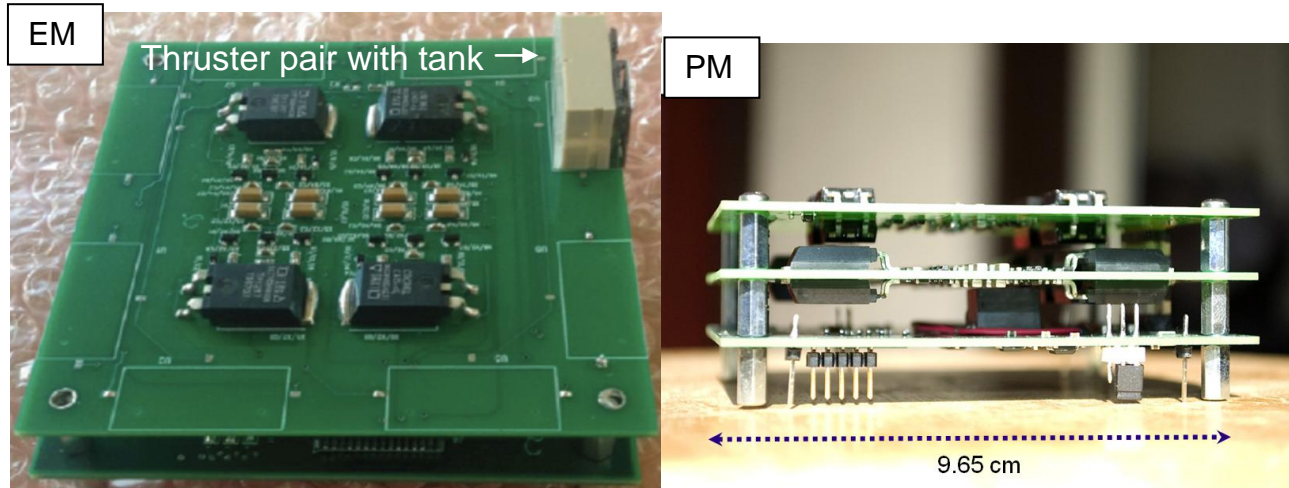


Figure 18. Left: Two-board engineering model. Right: Three-board prototype model, the lower portion of which would comprise the Lunar Impactor propulsion module power processing unit.

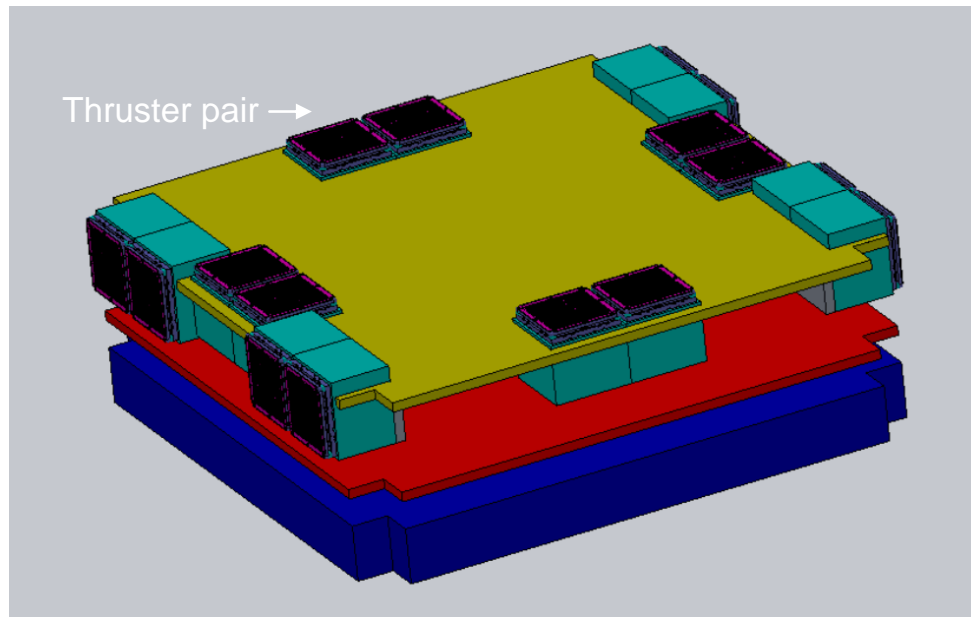


Figure 19. One notional thruster configuration for main propulsion and three-axis attitude control. The flight unit will have many more modules on the base panel for primary propulsion.

7. TRAJECTORY ANALYSIS – CUBESAT-ONLY APPROACH

7.1 Simulations

Ion electropray propulsion is highly efficient, but given the power constraints aboard the spacecraft, the thrust is very low. Maneuvers must be performed over long periods, and analysis methods for more traditional impulsive burns are not useful. Analytical solutions for low-thrust spacecraft trajectories can only be found in very limited cases; numerical simulation is the preferred method. The Astrogator module in STK is the tool of choice given its flexibility. All cases analyzed in the following section assume that the target point is the Reiner Gamma magnetic anomaly. It is also assumed that the initial wet mass of the cubesat is 5 kg and the specific impulse achieved is 2400 seconds.

Three initial conditions are considered: GEO, GTO, and Earth-Sun L1. For the GEO and GTO cases, both steady and variable thrust is simulated. Steady thrust represents a constant power supply to the thrusters (22.2 W after losses

translating to 1.6 mN of thrust) provided by articulated solar arrays, while variable thrust represents a non-constant power supply provided by body-mounted solar arrays (30 W after losses with optimal alignment). Thrust F is a linear function of input power P , $F = 2\eta P/c$. Thrust efficiency η is assumed to be 0.85, and c represents exhaust velocity. MATLAB plug-in scripts are used to compute the thrust and mass flow rate based on the power conditions, which depend on solar panel orientation. For power calculations, it is assumed that the thrust vector is always aligned with the velocity vector and that the vector normal to the main solar array is nadir-constrained. The power profile for the first 10 orbits is plotted in Fig. 20.

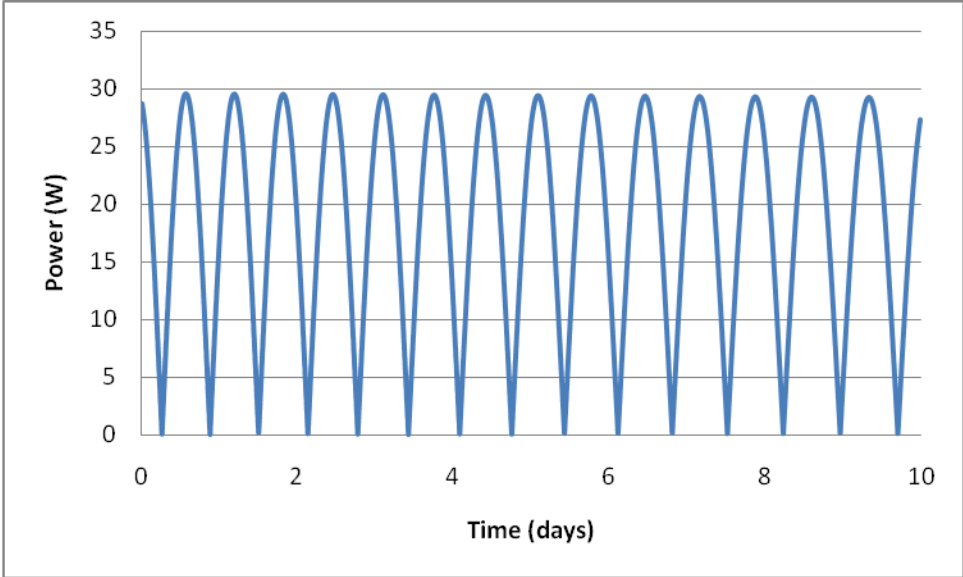


Figure 20. Power as a function of time over the first 10 days of thrusting.

Iterative techniques are used to find impact trajectories. Initial conditions are chosen such that the trajectory arrives near the desired point (Table 8), and a differential corrector is employed to refine the final conditions by adjusting the parameters of the last segment of the primary burn. The spacecraft coasts for the final segment, typically a few days, allowing for additional corrective burns should they be needed. The orbital inclination is not adjusted to match that of the Moon; rather, the initial conditions are such that the spacecraft encounters the Moon as it nears the equatorial plane. There is no need for high-rate attitude maneuvers as most of the thrusting is tangent to the velocity vector.

Table 8. Initial orbital parameters.

Initial value	GEO	GTO	Initial value	Earth-Sun L1
Time	06 Apr 2014 09:30:00	14 Apr 2014 08:00:00	Time	01 Apr 2014 18:00:00
a (km)	42164	24631.1	X (km, ECI)	1469090
e	0	0.705733	Y (km)	281764
i (deg)	0	0	Z (km)	122074
Ω (deg)	0	0	v_x (km/s)	-0.487449
ω (deg)	0	80	v_y (km/s)	0.701528
ν (deg)	0	0	v_z (km/s)	0.21642

7.2 Results and trades

It is difficult to impact Reiner Gamma at a low incidence angle due to its position on the lunar sphere. Equatorial plane spiral trajectories that intersect the Moon as it nears the ascending or descending node result in steep approaches because of the Moon’s gravitational influence and the incoming orbital velocity. Simple and direct trajectories like this optimize fuel, flight time, and radiation exposure, but the magnetic field readings are not very revealing. This is one of the key trades: propellant and time must be added to yield better scientific returns. Simpler trajectories are used for preliminary

analysis, but much attention is being paid to the examination of more aggressive flight plans to ensure that the incidence angle is low.

Increasing the demand on the propulsion system must be carefully considered. Greater Δv means longer firing times and higher probability of failure. The ion electrospray propulsion system will be flown in space before this mission occurs, but it will not be flight tested for the duration required by the Lunar Impactor. Longer flight time also means higher radiation exposure, which is already a concern.

The results obtained in the simulations are listed in Table 9. Note that these are preliminary, and the spacecraft does not have any form of feedback control. They are not optimized either; they meet basic mission objectives. Figures 21-23 show graphical representations of the GEO to Reiner Gamma trajectories.

It is evident that the GTO to Reiner Gamma cases are far more demanding on the propulsion system; this coupled with dozens of passes through the radiation belts makes it an unattractive option. In these cases, the spacecraft is powered down while transiting the most intense regions of the radiation belts. One must also note that using body-mounted arrays does not increase the flight time by unreasonable amounts. It has minimal impact on Δv and propellant usage as well.

Compensating for environmental perturbations is also a major consideration. Aside from gravitational forces, solar radiation pressure will have the most substantial effect. A rudimentary model is included in the current simulations, and this will be refined as the project continues. This model characterizes drift, but torques must be computed separately. Assuming a worst case center-of-pressure/center-of-gravity offset of 5 cm and a solar array area of 0.15 m, a torque of 6.86×10^{-8} Nm is applied (GEO to Reiner Gamma body-mounted array case). A single thruster module can provide torque on the order of 3×10^{-5} Nm depending on its configuration. Assuming constant countering of this torque by the thrusters over the course of the whole trajectory, a total Δv less than 1 m/s is required.

Attitude knowledge and control is a key driver of performance. Star trackers for cubesats are massive and occupy a large volume, so sun sensors are the primary option. However, they are less accurate, meaning thrust vector misalignment is likely to be greater. This will be thoroughly examined and characterized as work progresses. Preliminarily though, assuming a constant 2° thrust misalignment due to sensing errors, a total Δv of approximately 60 m/s is required for course corrections over the entire trajectory (GEO to Reiner Gamma body-mounted array case).

Future refinements to the trajectory simulations include incorporating pauses in thruster firing when in contact with the DSN and optimizing for incidence angle and radiation exposure. The optimal propellant mass fraction and specific impulse will be computed when the spacecraft mass is better defined. Robust simulations incorporating error and feedback control will be developed.

Table 9. Trajectory simulation results.

Initial Orbit	Solar Array Type	Time of Flight (days)	Propellant Consumed (grams)	Δv (km/s)
GEO*	Body-mounted	104	392	1.922
GEO*	Articulated	72	390	1.912
GTO	Body-mounted	172	624	3.138
GTO	Articulated	119	620	3.116
Earth-Sun L1	Articulated	74	134	0.639

*Primary option studied in this paper.

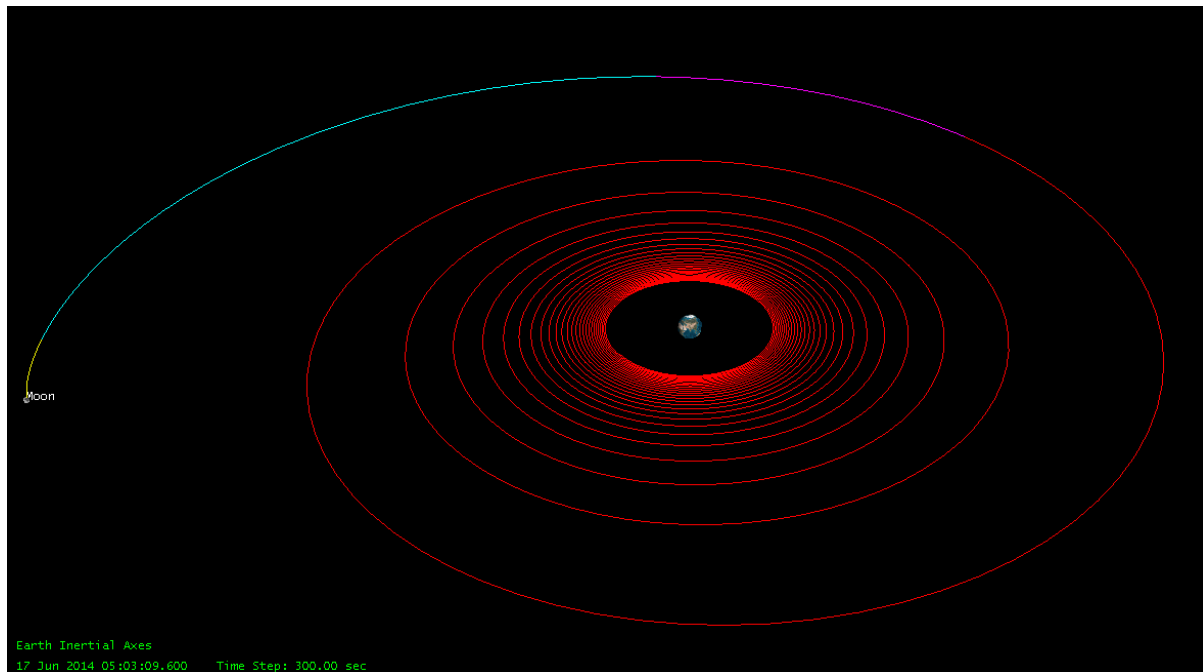


Figure 21. Trajectory from GEO to lunar impact. Blue and yellow segments are coasting periods.

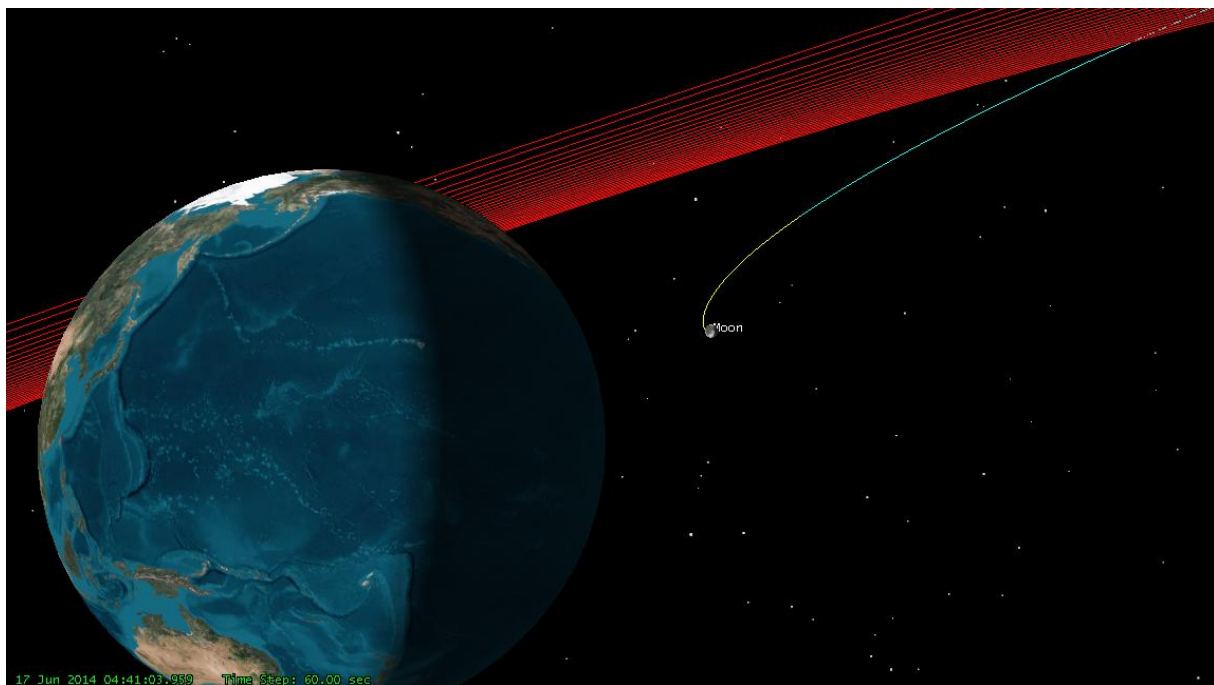


Figure 22. Geometry of the trajectory from GEO to lunar impact, as viewed from the Earth.

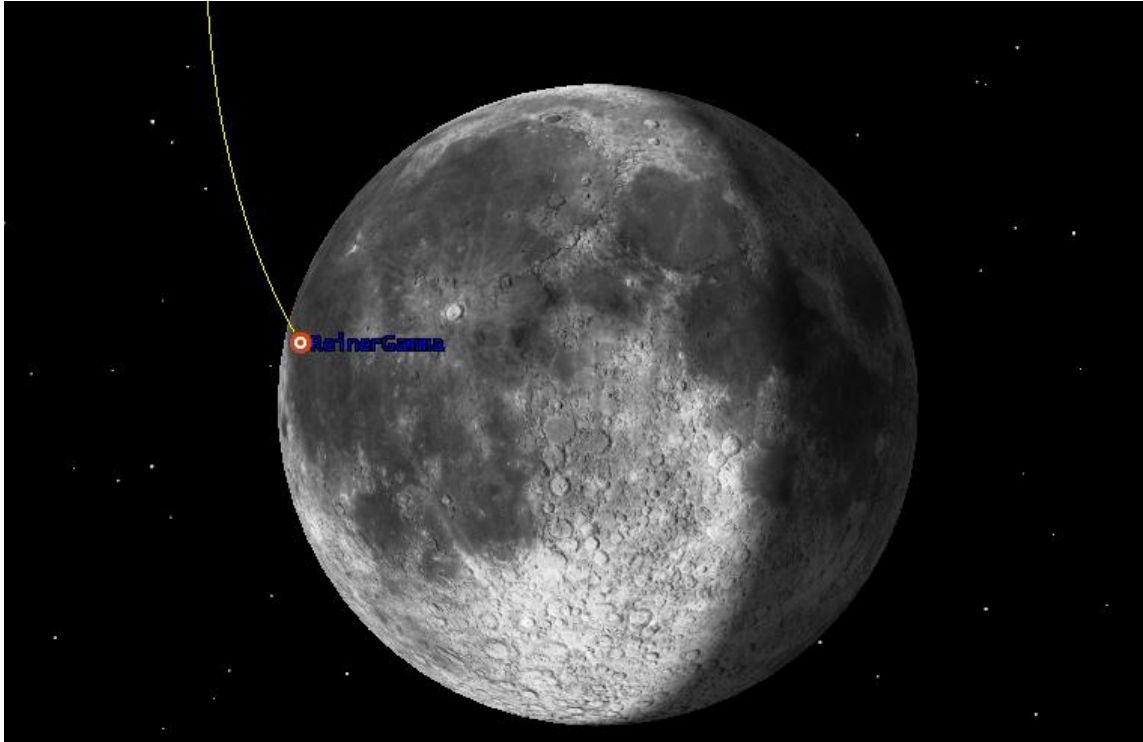


Figure 23. Close-up of the impact at Reiner Gamma, as viewed from an Earth-centered frame.

8. CONCLUSIONS

Our work shows that Lunar Impactor would perform important new measurements at lunar magnetic anomalies. The flight of such a mission will soon be feasible. For the cubesat-only approach, some of the technical challenges ahead include: 1) Long duration testing of the ion electrospray propulsion system, 2) Radiation mitigation techniques, 3) Refinement of the plan for accurate navigation to the Moon, and 4) Finding trajectories that impact the lunar surface at low angles, to maximize the science return. All of these challenges are surmountable and are being actively addressed. When Lunar Impactor is ready to fly, it will be a highly versatile platform capable of performing other near-Earth missions, such as unique observations of the magnetosphere and close-approaching asteroids.

ACKNOWLEDGEMENTS

This paper is dedicated to Bob Lin, our friend and mentor. This research was performed as part of the World Class University Project at Kyung Hee University, and sponsored by the Korean Ministry of Education, Science and Technology. IGB also thanks the Hellman Family Foundation for a Hellman Fellowship. We thank Clyde Space for permission to use their cubesat graphic in Figs. 3, 13 and 15. Authors are listed alphabetically after BAJ.

REFERENCES

- [1] Fuller, M., and Cisowski, S. M., "Lunar paleomagnetism," *Geomagnetism*, 2, 307-455 (1987).
- [2] Wieczorek, M. A., Jolliff, B. L., Khan, A. *et al.*, "The constitution and structure of the lunar interior," *Rev. Mineral. Geochem.*, 60, 221-364 (2006).
- [3] Garrick-Bethell, I., Weiss, B. P., Shuster, D. L. *et al.*, "Early lunar magnetism," *Science*, 323, 356-359 (2009).
- [4] Shea, E. K., Weiss, B. P., Cassata, W. S. *et al.*, "A long-lived lunar core dynamo," *Science*, 335, 453-456 (2012).

- [5] Dwyer, C. A., Stevenson, D. J., and Nimmo, F., "A long-lived lunar dynamo driven by continuous mechanical stirring," *Nature*, 470, 212-214 (2011).
- [6] Le Bars, M., Wicczorek, M., Karatekin, O. *et al.*, "An impact-driven dynamo for the early Moon," *Nature*, 479, 215-218 (2011).
- [7] Hood, L. L., and Artemieva, N. A., "Antipodal effects of lunar basin-forming impacts: Initial 3-D simulations and comparisons with observations," *Icarus*, 193, 485-502 (2008).
- [8] Hood, L. L., and Schubert, G., "Lunar magnetic anomalies and surface optical properties," *Science*, 208, 49-51 (1980).
- [9] Hemingway, D., and Garrick-Bethell, I., "Magnetic field direction and lunar swirl morphology: Insights from Airy and Reiner Gamma," *J. Geophys. Res.*, 117, E10012 (2012).
- [10] Hapke, B., "Space weathering from Mercury to the Asteroid Belt," *J. Geophys. Res.*, 106, 10039-10073 (2001).
- [11] Criswell, D. R., "Lunar dust motion," *Proc. Lunar Sci. Conf. 3rd*, 2671-2680 (1972).
- [12] Colwell, J. E., Robertson, S. R., Horányi, M. *et al.*, "Lunar dust levitation," *J. Aero. Eng.*, 22, 2-9 (2009).
- [13] Garrick-Bethell, I., Head, J. W., and Pieters, C. M., "Magnetic fields, spectral properties, and dust transport at lunar swirls," *Icarus*, 212, 480-492 (2011).
- [14] Kramer, G. Y., Besse, S., Dhingra, D. *et al.*, "M3 spectral analysis of lunar swirls and the link between optical maturation and surface hydroxyl formation at magnetic anomalies," *J. Geophys. Res.*, 116, E00G18 (2011).
- [15] Pieters, C. M., Goswami, J. N., Clark, R. N. *et al.*, "Character and Spatial Distribution of OH/H₂O on the Surface of the Moon Seen by M³ on Chandrayaan-1," *Science*, 326(5952), 568-572 (2009).
- [16] Saito, Y., Yokota, S., Tanaka, T. *et al.*, "Solar wind proton reflection at the lunar surface: Low energy ion measurement by MAP-PACE onboard SELENE (KAGUYA)," *Geophys. Res. Lett.*, 35, L24205 (2009).
- [17] Saito, Y., Nishino, M. N., Fujimoto, M. *et al.*, "Simultaneous observation of the electron acceleration and ion deceleration over lunar magnetic anomalies," *Earth Planets Space*, 64, 83-92 (2012).
- [18] Poppe, A. R., Halekas, J., Delory, G. T. *et al.*, "Particle in cell simulations of the solar wind interaction with lunar crustal magnetic anomalies: Magnetic cusp regions," *J. Geophys. Res.*, 117, A09105 (2012).
- [19] Purucker, M., and Nichols, J., "Global spherical harmonic models of the internal magnetic field of the Moon based on sequential and coestimation approaches," *J. Geophys. Res.*, 115, E12007 (2010).
- [20] Stutzke, N., Russek, S. E., Pappas, D. P. *et al.*, "Low frequency noise measurements on commercial magnetoresistive magnetic field sensors," *J. Appl. Phys.*, 97, 10Q107 (2005).
- [21] Carr, C., "The Double Star magnetic field investigation: Overview of instrument performance and initial results," *Ann. Geophys.*, 23, 2713-2732. (2005).
- [22] Lee, Y., Jin, H., Seon, J. *et al.*, "Development of CubeSat for space science mission: CINEMA," *Proc. 62nd International Astronautical Congress*, paper IAC-11-B4.2.5 (2011).
- [23] Liu, L.-Y., Jiang, S.-B., Yeh, T.-L. *et al.*, "The Magneto-Resistive Magnetometer of BCU on the Tatiana-2 Satellite," *Terrestrial, Atmospheric and Oceanic Sciences*, 23.3, 70-79 (2012).
- [24] Brown, P., Beek, T., Carr, C. *et al.*, "Magnetoresistive magnetometer for space science applications," *Meas. Sci. Tech.*, 23, 025902 (2012).
- [25] Sanz, R., Fernandez, A. B., Dominguez, J. A. *et al.*, "Gamma Irradiation of Magnetoresistive Sensors for Planetary Exploration," *Sensors*, 12, 4447-4465 (2012).
- [26] Duncan, C. B., "Low Mass Radio Science Transponder - Navigation Anywhere," *Proc. iCubeSat 2012 Interplanetary CubeSat Workshop*, Paper C.3.2 (2012).
- [27] Bester, M., Lewis, M., Roberts, B. *et al.*, "Multi-mission Flight Operations at UC Berkeley – Experiences and Lessons Learned," *Proc. AIAA SpaceOps Conference*, Paper AIAA-2010-2198 (2010).
- [28] Cosgrove, D., Frey, S., Folta, D. *et al.*, "Navigating THEMIS to the ARTEMIS Low-Energy Lunar Transfer Trajectory," *Proc. AIAA SpaceOps Conference*, Paper AIAA-2010-2352 (2010).
- [29] Cosgrove, D., Owens, B., Marchese, J. *et al.*, "ARTEMIS Operations from Earth-Moon Libration Orbits to Stable Lunar Orbits," *Proc. AIAA SpaceOps Conference*, Paper AIAA 2012-1296179 (2012).
- [30] Roberts, B., Lewis, M., Thorsness, J. *et al.*, "THEMIS Mission Networks Expansion – Adding the Deep Space Network for the ARTEMIS Lunar Mission Phase," *AIAA SpaceOps Conference*, Paper AIAA-2010-1934 (2010).
- [31] Kinman, P. W., [Deep Space Network Telecommunications Link Design Handbook, 810-005, Revision E] NASA Jet Propulsion Laboratory, Pasadena, CA(2009).
- [32] Lozano, P., "Ionic Liquid Ion Sources: Suppression of Electrochemical Reactions using Voltage Alternation," *Journal of Colloid and Interface Science*, 280(1), 149-154 (2004).

- [33] Legge, R. S., and Lozano, P., "Electrospray Propulsion Based on Emitters Microfabricated in Porous Metals," *Journal of Propulsion and Power*, 27(2), 485-495 (2011).
- [34] Courtney, D., and Lozano, P., "Electrochemical Micromachining on Porous Nickel for Arrays of Electrospray Ion Emitters," *Journal of Microelectromechanical Systems*, 22(2), 471-482 (2012).